Clinical system for non-invasive *in situ* monitoring of gases in the human paranasal sinuses

Märta Lewander[1], Zuguang Guan[1], Katarina Svanberg[2], Sune Svanberg[1], and Tomas Svensson[1]

[1]*Department of Physics, Lund University, Sweden*

[2]*Department of Oncology, Lund University Hospital, Sweden*

marta.lewander@fysik.lth.se

Abstract: We present a portable system for non-invasive, simultaneous sensing of molecular oxygen (O_2) and water vapor (H_2O) in the human paranasal cavities. The system is based on high-resolution tunable diode laser spectroscopy (TDLAS) and digital wavelength modulation spectroscopy (dWMS). Since optical interference and non-ideal tuning of the diode lasers render signal processing complex, we focus on Fourier analysis of dWMS signals and procedures for removal of background signals. Clinical data are presented, and exhibit a significant improvement in signal-to-noise with respect to earlier work. The *in situ* detection limit, in terms of absorption fraction, is about 5×10^{-5} for oxygen and 5×10^{-4} for water vapor, but varies between patients due to differences in light attenuation. In addition, we discuss the use of water vapor as a reference in quantification of *in situ* oxygen concentration in detail. In particular, light propagation aspects are investigated by employing photon time-of-flight spectroscopy.

OCIS codes: (170.4940) Otolaryngology; (170.1610) Clinical applications; (170.3890) Medical optics instrumentation; (170.6510) Spectroscopy, tissue diagnostics; (300.6260) Spectroscopy, diode lasers; (300.6320) Spectroscopy, high-resolution; (170.7050) Turbid media; (170.5280) Photon migration; (300.6500) Spectroscopy, time-resolved

References and links

1. P. Martin, "Near-infrared diode laser spectroscopy in chemical process and environmental air monitoring," Chem. Soc. Rev. **31**, 201–210 (2002).
2. I. Linnerud, P. Kaspersen, and T. Jæger, "Gas monitoring in the process industry using diode laser spectroscopy," Appl. Phys. B **67**, 297–305 (1998).
3. G. Galbacs, "A review of applications and experimental improvements related to diode laser atomic spectroscopy," Appl. Spectrosc. Rev. **41**, 259–303 (2006).
4. M. Sjöholm, G. Somesfalean, J. Alnis, S. Andersson-Engels, and S. Svanberg, "Analysis of gas dispersed in scattering media," Opt. Lett. **26**, 16–18 (2001).
5. T. Svensson, M. Andersson, L. Rippe, J. Johansson, S. Folestad, and S. Andersson-Engels, "High sensitivity gas spectroscopy of porous, highly scattering solids," Opt. Lett. **33**, 80–82 (2008).
6. J. Alnis, B. Anderson, M. Sjöholm, G. Somesfalean, and S. Svanberg, "Laser spectroscopy of free molecular oxygen dispersed in wood materials," Appl. Phys. B **77**, 691–695 (2003).
7. T. Svensson, M. Andersson, L. Rippe, S. Svanberg, S. Andersson-Engels, J. Johansson, and S. Folestad, "VCSEL-based oxygen spectroscopy for structural analysis of pharmaceutical solids," Appl. Phys. B **90**, 345–354 (2008).

#109769 - $15.00 USD Received 7 Apr 2009; revised 4 May 2009; accepted 5 May 2009; published 15 Jun 2009

8. L. Persson, M. Andersson, M. Cassel-Engquist, K. Svanberg, and S. Svanberg, "Gas monitoring in human sinuses using tunable diode laser spectroscopy," J. Biomed. Opt. **12**, 054,001 (2007).
9. T. Svensson, "Pharmaceutical and biomedical applications of spectroscopy in the photon migration regime," PhD Thesis, Lund University (2008). URL `www.atomic.physics.lu.se/biophotonics/publications/phd_theses`.
10. S. Svanberg, "Gas in scattering media absorption spectroscopy - GASMAS," Proc. SPIE **7142**, 714202 (2008).
11. J. A. Silver, "Frequency-modulation spectroscopy for trace species detection: theory and comparison among experimental methods," Appl. Opt. **31**, 707–717 (1992).
12. P. Kluczynski, J. Gustafsson, Å. Lindberg, and O. Axner, "Wavelength modulation absorption spectrometry - an extensive scrutiny of the generation of signals," Spectrochim. Acta B **56**, 1277–1354 (2001).
13. T. Fernholz, H. Teichert, and V. Ebert, "Digital, phase-sensitive detection for in situ diode-laser spectroscopy under rapidly changing transmission conditions," Appl. Phys. B **75**, 229–236 (2002).
14. M. Andersson, L. Persson, T. Svensson, and S. Svanberg, "Flexible lock-in detection system based on synchronized computer plug-in boards applied in sensitive gas spectroscopy," Rev. Sci. Instrum. **78**, 113,107 (2007).
15. W. Fokkens, V. Lund, and J. Mullol, "European position paper on rhinosinusitis and nasal polyps 2007," Rhinol. Suppl. **20**, 1–136 (2007).
16. C. Bachert, K. Hormann, R. Mosges, G. Rasp, H. Riechelmann, R. Muller, H. Luckhaupt, B. A. Stuck, and C. Rudack, "An update on the diagnosis and treatment of sinusitis and nasal polyposis," Allergy **58**, 176–191 (2003).
17. L. Persson, M. Andersson, T. Svensson, M. Cassel-Engquist, K. Svanberg, and S. Svanberg, "Non-intrusive optical study of gas and its exchange in human maxillary sinuses," Proc. SPIE **6628**,662804 (2007).
18. L. Persson, M. Lewander, M. Andersson, K. Svanberg, and S. Svanberg, "Simultaneous detection of molecular oxygen and water vapor in the tissue optical window using tunable diode laser spectroscopy," Appl. Opt. **47**, 2028–2034 (2008).
19. "Application Note 1040: Coherent Sampling vs. Window Sampling," Tech. rep., Maxim (2002).
20. A. Buck, "New equations for computing vapor-pressure and enhancement factor," J. Appl. Meteorol. **20**, 1527–1532 (1981).
21. T. Svensson, E. Alerstam, M. Einarsdóttír, K. Svanberg, and S. Andersson-Engels, "Towards accuracte in vivo spectroscopy of the human prostate," J. Biophoton. **1** 200–203 (2008).
22. E. Alerstam, S. Andersson-Engels, and T. Svensson, "Improved accuracy in time-resolved diffuse reflectance spectroscopy," Opt. Express **16**, 10,434–10,448 (2008).
23. B. Chance, J. Leigh, H. Miyake, D. Smith, S. Nioka, R. Greenfeld, M. Finander, K. Kaufmann, W. Levy, M. Young, P. Cohen, H. Yoshioka, and R. Boretsky, "Comparison of time-resolved and time-unresolved measurements of deoxyhemoglobin in brain," P. Natl. Acad. Sci. USA **85**, 4971–4975 (1988).
24. R. Engelbrecht, "A compact NIR fiber-optic diode laser spectrometer for CO and CO_2: analysis of observed 2f wavelength modulation spectroscopy line shapes," Spectrochim. Acta A **60**, 3291–3298 (2004).

1. Introduction

High-resolution tunable diode laser absorption spectroscopy (TDLAS) is a powerful tool for selective and sensitive gas sensing, and is widely used in science and technology [1, 2, 3]. The conventional experimental configuration involves either open path monitoring or gas cells (single or multi-pass), while data evaluation typically relies on lineshape theory in combination with the Beer-Lambert-Bouguer law of light transmission. In 2001, it was demonstrated that TDLAS can be used also for sensing of gases inside porous and highly scattering (turbid) solids [4]. In contrast to the conventional conditions described above, measurements of gases in pores of solids involve working with diffuse light, heavy attenuation, severe optical interference and unknown optical pathlengths [5]. To emphasize these unusual and aggravating experimental conditions, the technique is often separately termed *gas in scattering media absorption spectroscopy* (GASMAS). The technique has been used to characterize various porous materials, such as polystyrene foam [4], wood [6], pharmaceutical tablets [7], and human sinus cavities [8]. Reviews of GASMAS are available in Refs. [9, 10].

A fundamental aspect of GASMAS is the great contrast between the spectrally sharp absorption lines of free gases (lines used in this work are about 0.006 nm FWHM) and the slowly varying absorption spectra of solids. This contrast allows detection of weak gas absorption even under heavy background absorption. So far, GASMAS has been used to detect molecular oxygen (O_2) at around 760 nm, or water vapour (H_2O) around 935 or 980 nm. Since

#109769 - $15.00 USD Received 7 Apr 2009; revised 4 May 2009; accepted 5 May 2009; published 15 Jun 2009

the corresponding absorption lines are weak, GASMAS has relied on wavelength modulation spectroscopy (WMS) to increase sensitivity. WMS is a well established tool in TDLAS [11], and involves sinusoidal modulation of the laser wavelength and detection at harmonics of the modulation frequency (detection at the second harmonic, $2f$, is a common choice). The WMS technique shifts the absorption signal to a frequency range less affected by low-frequency noise of system components, and allows baseline-free recordings of derivative-like versions of the actual absorption feature [12, 9]. Traditionally, WMS relies on analog function generators for laser modulation, lock-in amplifiers for detection of signal harmonics, and oscilloscopes for data acquisition. By synchronizing data acquisition with function generators for laser modulation, it is possible to simultaneous record multiple WMS harmonics without the need of lock-in amplifiers [13]. The WMS system can be further simplified by employing a single plug-in board with synchronized outputs and inputs for laser modulation and data acquisition [14]. These approaches can be termed digital wavelength modulation spectroscopy (dWMS), and is based on recording of the raw detector signals. Equivalents to the traditional WMS signal, as generated by a lock-in amplifier, are obtained by employing a digital lock-in amplifier (*e.g.* the LabVIEW lock-in toolkit) [14] or by means of Fourier analysis [13, 7].

Diagnostics of the human sinuses is a particularly interesting application of the GASMAS technique [8]. The maxillary and frontal sinuses are located behind the cheek bones and the frontal bone, respectively. In a healthy state the sinuses are air filled cavities ventilated through the nasal ventricle. Sinusitis, now often termed rhinosinusitis, is an infection of the sinuses, causing nasal blockage and mucus obstruction [15]. Current diagnostic methods of the paranasal sinuses include case history and, in selected cases, computed tomography (CT) [16]. The diagnostic potential of the GASMAS technique has been demonstrated on volunteers with a laboratory system for oxygen spectroscopy [17, 8]. As discussed in Ref. [8], the diagnostic value of the approach may be significantly increased by incorporating simultaneous sensing of both water vapor and molecular oxygen. The reason is that cavities in the human body often can be assumed to be at 37 °C and at 100% relative humidity, and that the *in situ* concentration of water vapor thus can be considered known. Assuming that the optical pathlength through the gas-filled cavity is the same at 760 nm and 935 nm, the water vapor data can then provide the information on optical pathlength needed to estimate the *in situ* oxygen concentration. Sequential sensing of H_2O and O_2 in human sinuses has been demonstrated using a laboratory setup based on traditional, analog WMS [8].

In this work, we present a portable system designed for a clinical trial aimed at monitoring gas in the paranasal sinuses of 40 patients undergoing investigation for sinus-related problems. The system is based on dWMS, and allow simultaneous sensing of H_2O and O_2. The clinical performance is significantly better than previous reported clinical work [18] (tenfold improvement in signal-to-noise). We report our experiences from using pigtailed diode lasers and optical fibers in TDLAS instruments, and the signal processing required to reach the improved performance is described in detail. In addition, for the first time, we employ photon time-of-flight spectroscopy (PTOFS) to investigate the photon migration aspects of optical sinus diagnostics. By estimating photon pathlengths at 786 nm and 916 nm, we can scrutinize the idea of using the water vapor absorption at 935 nm to estimate optical pathlength at 760 nm. Finally, we discuss the possibility of constructing a simpler TDLAS system for monitoring of gas in the paranasal sinuses.

2. Materials and methods

2.1. TDLAS instrumentation

The TDLAS system for our clinical application is a fiber-based dual beam system based on coherent sampling and digital wavelength modulation spectroscopy (dWMS). A schematic of

#109769 - $15.00 USD Received 7 Apr 2009; revised 4 May 2009; accepted 5 May 2009; published 15 Jun 2009

the instrumentation is given in Fig. 1. The wavelength of two pigtailed DFB lasers (Nanoplus, Germany) are scanned across single absorption lines of molecular oxygen (at 760.445 nm, peak absorption 2.6×10^{-5} mm^{-1} for 21% O_2) and water vapor (at 935.686 nm, peak absorption 2.4×10^{-4} mm^{-1} for H_2O at 100% relative humidity and 37 °C). Diode laser modulation and data acquisition is managed by a PCI board with synchronized outputs and outputs (NI-6120, National Instruments). The modulation consists of a $f_{scan} = 5$ Hz triangular waveform for wavelength scanning together with a faster sinusoidal waveform for wavelength modulation. The amplitude of the wavelength modulation is chosen so that the $2f$ harmonics are maximized, *i.e.* set to 2.2 times the absorption linewidth (half width at half maximum). Straightforward separation of the two absorption signals is ensured by choosing different modulation frequencies, f_m, for the wavelength modulation of the two lasers (9,015 and 10,295 Hz for the oxygen and water vapor lasers, respectively) [18]. Modulation signals are sent to two diode laser drivers (06DLD103, Melles Griot), which are used to operate injection currents as well as for temperature stabilization.

Severe optical interference originating from optical components makes single beam TDLAS operation unfeasible. Instead, single mode optical fiber couplers are used to create a dual beam configuration (sample and reference arms). The output from the two pigtailed diode lasers are about 4 mW each. Due to non-ideal performance of these couplers, the optical powers available in the sample arm are only 0.25 mW (935 nm) and 1 mW (760 nm). A fiber probe is used to inject light into the tissue, and a 18×18 mm^2 unbiased large-area photodiode (S3204-8, Hamamatsu) is used to detect transmitted diffuse light. Light in the reference arm is detected by a 10×10 mm^2 unbiased photodiode (S3590-01, Hamamatsu). Low-noise transimpedance amplifiers (DLPCA-200, FEMTO Messtechnik, Germany) convert photodiode currents, and the amplification is typically set to 10^6 or 10^7 V/A in clinical measurements. The resulting voltage signals are coherently sampled at f_s=400,000 samples/s by the PCI board. Averaged voltage data are stored on disc and post-processing of data is required to obtain absorption imprints. Each dataset corresponds to one full period of the scan frequency, *i.e.* 80,000 samples (and is in general a result of averaging over several scans). The signal processing is described in detail in the following section. Note that both modulation frequencies, as well as the scan frequency, satisfy the criteria for coherent sampling (*i.e.* an integer number of cycles are sampled) [19].

2.2. Signal processing

As described in the previous section, the system stores an amplified version of the raw photodiode output. In contrast to conventional WMS, where a lock-in amplifier is used to monitor a single frequency channel, this means that the data contains information on multiple harmonics, as well as on detected intensities. For the case of single beam setups, Fourier methods for extracting WMS signals from such data have been described by Fernholz *et al.* [13] and Svensson *et al.* [7]. However, due to complex background signals, the dual beam data generated by the system used in this work requires special treatment. A detailed description of the signal processing is therefore given below.

An example of acquired raw data from the sample arm, $u_s(t)$, and its corresponding Fourier spectrum is shown in Fig. 2. Data from the two arms, *i.e.* $u_s(t)$ and $u_r(t)$, are processed in similar ways, and we therefore drop the subscripts in steps that apply for both signals. The initial processing steps are performed in the Fourier domain (Eq. 1).

$$U(\omega) = \mathscr{F}\{u(t)\} \tag{1}$$

As can be seen in Fig. 2, individual harmonics of the modulation frequencies appear as separated peaks in the Fourier spectrum. In order to study a specific harmonic n of a specific modulation frequency ω_m, the signal simply needs to be bandpass filtered. The bandpass filter-

#109769 - $15.00 USD Received 7 Apr 2009; revised 4 May 2009; accepted 5 May 2009; published 15 Jun 2009

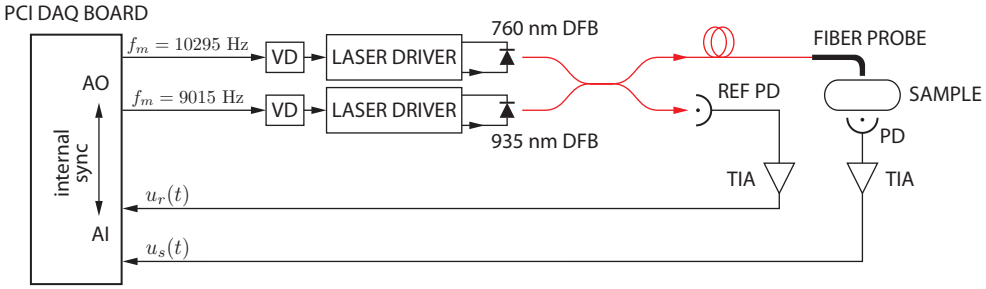

Fig. 1. A schematic of the instrumentation. A PCI board with synchronized analog outputs (AO) and analog inputs (AI) manages both laser modulation and data acquisition. In order to utilize the full dynamic range of the AO, voltage dividers (VD) are used to reduce the signal level before modulation signals reach the diode laser drivers. Simultaneous sensing of O_2 and H_2O is achieved by using two pigtailed DFB diode lasers operating around 760 nm and 935 nm, respectively. In order to allow separation of the two corresponding absorption signals, the two lasers are operated at different modulation frequencies, f_m. The laser outputs are arranged in a dual beam configuration: one photodiode (PD) provides the reference signal, and a second records a signal carrying gas absorption information. Transimpedance amplifiers (TIA) convert and amplify the photodiode currents, and the resulting voltages are coherently sampled and averaged.

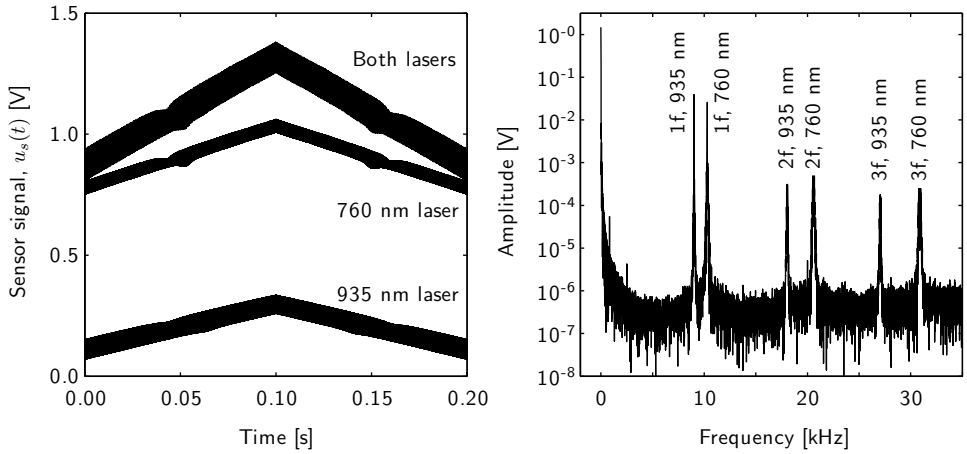

Fig. 2. Raw data exemplified by a measurement on a 1000 mm path through ambient air. Two lasers contribute to the detected signal, and the individual contributions and their sum are shown in (left). A single-sided amplitude spectrum of the full signal (both lasers) is given in (right), showing 1-3f WMS components due to interactions with absorption features. Note that the $1f$ components are dominated by residual amplitude modulation (RAM) of the diode lasers (see text for a discussion on RAM).

#109769 - $15.00 USD Received 7 Apr 2009; revised 4 May 2009; accepted 5 May 2009; published 15 Jun 2009

ing is achieved in the frequency domain by using a super-Gauss window centered at $+\omega_m$ with the width $\delta\omega$. The operation is stated in Eq. 2 (where the factor 2 is included to compensate for the signal amplitude lost by neglecting the negative frequencies), and the resulting signal is denoted $U_{nf}(\omega)$.

$$U_{nf}(\omega) = 2 \times U(\omega) \times \exp\left(-\left(\frac{\omega - n \times \omega_m}{\delta\omega} \right)^8 \right) \tag{2}$$

In order to study the evolution of ω_m frequency content as the laser is scanned, we down-convert ω_m to zero frequency,

$$V_{nf}(\omega) = U_{nf}(\omega + n \cdot \omega_m), \tag{3}$$

and perform a subsequent inverse Fourier transformation:

$$v^*_{nf}(t) = \mathscr{F}^{-1}\{V_{nf}(\omega)\}. \tag{4}$$

The resulting time-dependent signal, $v^*_{nf}(t)$, is complex valued and can be studied in phase-amplitude plots (a plot of the real versus the imaginary part) [13, 7]. In a phase-amplitude plot, a pure sinusoidal signal will thus appear as a single dot. The signal amplitude is given by the distance to the origin, and its phase is given by the angle with respect to *e.g.* the real axis. In WMS experiments, the strength of harmonics vary as the laser is scanned across an absorption feature (or other transmission profiles). In the ideal case (linear tuning characteristics), the phase-amplitude plot will therefore show values along a line (pure amplitude changes and 180° phase jumps). For the $1f$ harmonic, the line will have a significant offset due to the residual amplitude modulation (RAM) of the laser diode (modulation of the laser frequency is accompanied by power modulation). For higher harmonics, WMS is ideally free from baseline, and the line will therefore cross the origin. It is important to realize that a phase-amplitude plot with values along a line does not guarantee a good signal-to-noise ratio. The reason is that all transmission profiles, not only gas absorption, will give rise to line-type phase-amplitude plots (including etalon fringes and other interference effects that typically limit TDLAS).

Before taking a look at experimental signals, it is, however, useful to make some additional processing. In order to reach a quantitatively relevant signal, it is necessary to perform intensity correction (signals are proportional to the detected intensity). The detected signal is, however, a sum of the contributions from the two lasers (wavelengths). In order to determine the individual contribution of a specific light source, we use the $1f$ RAM of the lasers. Since the two laser are modulated using different frequencies, the $1f$ RAM signals are easily distinguished (and given by the average of $v^*_{1f}(t)$). The exact procedure for intensity correction is stated in Eq. 5, and the resulting normalised quantity is denoted $\overline{v}^*_{nf}(t)$. Note that a time-dependent calibration factor, $k(t)$, is introduced and used to convert the $1f$ RAM into a measure of average signal level and its evolution as the laser is scanned. This manoeuver makes it possible to compare obtained signal levels with WMS theory (*e.g.* that the $2f$ WMS peak signals should corresponds to about 0.3 times the actual absorption fraction). Note also, that the procedure includes removal of offsets (these are not of any diagnostic value in subsequent analysis).

$$\overline{v}^*_{nf}(t) = \frac{v^*_{nf}(t) - \text{mean}(v^*_{nf}(t))}{k(t) \times \text{mean}(v^*_{1f}(t))}. \tag{5}$$

Figure 3 shows 1-3f phase-amplitude plots originating from interactions with an absorption line of molecular oxygen. As can be seen in the left column, strong absorption results in the expected line-type phase-amplitude plots. The middle column shows sample arm data from experiments on L=2 cm ambient air, giving an absorption fraction typical to that encountered in the clinical experiments. There, the phase-amplitude plot no longer exhibit the line-type structure expected in ideal WMS experiments. In order to emphasize this, the figure compares data

#109769 - $15.00 USD Received 7 Apr 2009; revised 4 May 2009; accepted 5 May 2009; published 15 Jun 2009

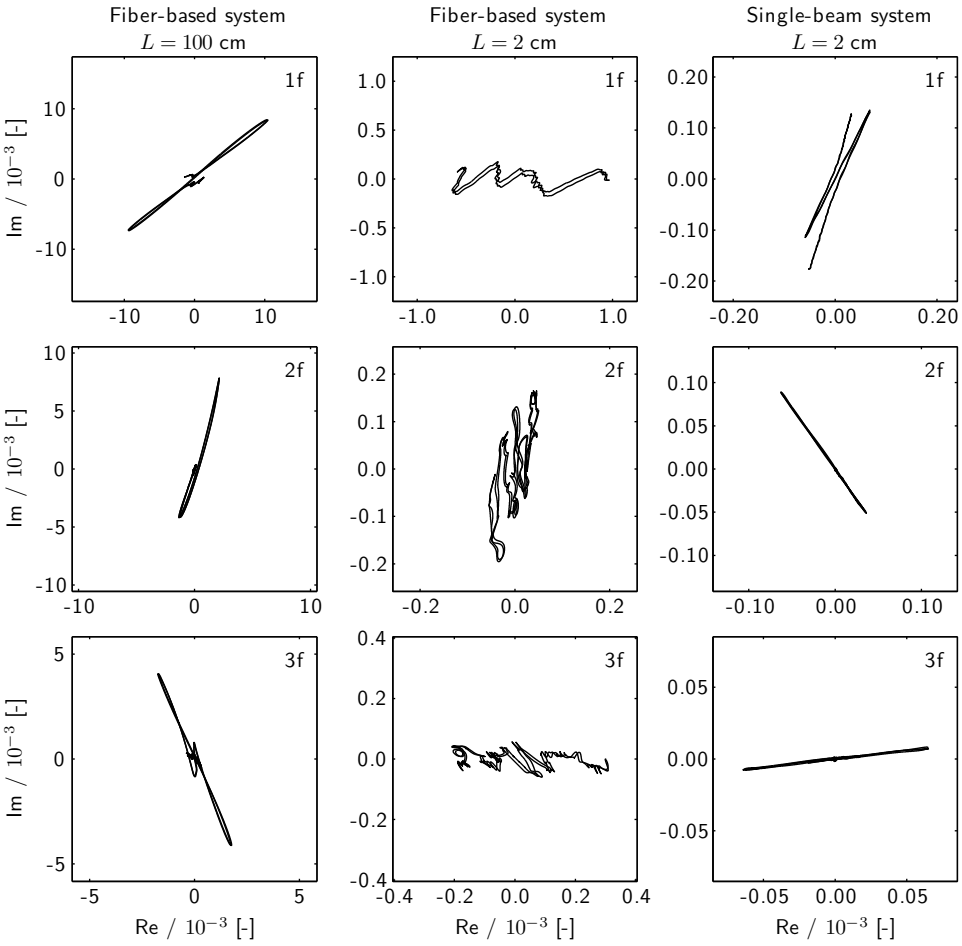

Fig. 3. Phase-amplitude plots of sample arm $\overline{v}^{*}_{nf}(t)$-signals originating from ambient air (free-space) measurements. In order to show the signal structure, offsets have been removed. For the fiber-based system used in the present work, large absorption is required to produce a line-type phase-amplitude plot (left column, L=100 cm pathlength through ambient air, 3×10^{-2} absorption fraction). In the case of low absorption, the phase plot is completely dominated by background effects (middle column, L=2 cm, 5×10^{-4} absorption fraction). In contrast, single beam operation without optical fibers results in line-type phase-amplitude plots even at low absorption (right column, L=2 cm, optical system as in Ref. [5] while data acquisition and laser control is managed by the system presented in this paper).

#109769 - $15.00 USD Received 7 Apr 2009; revised 4 May 2009; accepted 5 May 2009; published 15 Jun 2009

obtained using the fiber-based system (left and middle columns) with data obtained using an optical system that involves nothing but a VCSEL diode laser and a photodiode (right column). When utilizing our fiber-based setup, the observed signal structure is a complex result of non-ideal laser tuning, interference fringes and gas absorption. In order to extract the often minor contribution from gas absorption, we have developed a scheme for subtraction of background effects. We assume that the signal registered in the sample arm, $\overline{\nu}_s^*$, can be described by a combination of the simultaneously recorded reference arm signal, $\overline{\nu}_r^*$, and a so called absolute reference recording of a strong, well-known gas absorption, $\overline{\nu}_{a.r.}^*$ (recorded using the same system, but not simultaneously). In this work, the absolute reference originates from measurements in ambient air ($L_{a.r.} = 1$ m for evaluation of clinical data). The model is explicitly stated in Eq. 6 (note that the nf-subscript has been dropped).

$$\overline{\nu}_s^*(t) \simeq p^*(t) + q^*(t) \times \overline{\nu}_r^*(t) + c \times \overline{\nu}_{a.r.}^*(t - t_0). \tag{6}$$

Here, $p^*(t)$ and $q^*(t)$ are complex polynomials introduced to handle baseline differences between the reference and sample arms. c is a real coefficient and gives the fraction of the absolute reference needed to explain the gas absorption registered in the sample arm. Phase difference between new experimental data and absolute reference recording can be handled by replacing c with a complex valued coefficient (c^*). Such differences can occur due to changes in ambient temperature and diode laser operation settings. Differences in the location of the absorption within the scan is accounted for by introducing the shift parameter t_0. The best model fit is determined by means of non-linear Levenberg-Marquardt optimization on t_0 (note that for a given t_0, the optimization problem reduces to linear regression). The absorption signal, $\overline{w}^*$, is reached after subtraction of fitted background signals:

$$\overline{w}^*(t) = \overline{\nu}_s^*(t) - p_{\text{fit}}^*(t) + q_{\text{fit}}^*(t) \times \overline{\nu}_r^*(t) \tag{7}$$

A conventional WMS signal is reached by determining the signal phase, β_n, and extracting the amplitude variation, as stated in Eq. 8.

$$WMS_{nf}(t) = \text{Real}\left\{ \left(\overline{w}_{nf}^*(t) - \text{mean}\left(\overline{w}_{nf}^*(t)\right) \right) \times \exp(-i\beta_n) \right\} \tag{8}$$

Figure 4 illustrates the importance of background subtraction, showing model fits and resulting WMS signals. As customary in GASMAS, experimental signals are measured in terms of equivalent pathlength in ambient air, L_{eq}. If needed, a superscript is used to differentiate between water vapor, $L_{eq}^{H_2O}$, and oxygen signals, $L_{eq}^{O_2}$. When evaluation is performed using the scheme described above, the L_{eq} is related to the pathlength used in the recording of the absolute reference, $L_{a.r.}$, as stated in Eq. 9.

$$L_{eq} = c_{\text{fit}} \times L_{a.r.} \tag{9}$$

While the concentration of molecular oxygen in air can be assumed fixed at 21%, the abundance of water vapor varies strongly with temperature and relative humidity. In this work, water vapor signals are measured with respect to equivalent pathlength in air at 37 °C and 100% relative humidity, *e.g.* the condition expected in cavities of the human skull. The absolute reference recording used in evaluation of water vapor absorption is measured in ambient air, simultaneous to the recording of an absolute reference for oxygen. The water vapor concentration in these experiments is inferred from measurements of temperature and relative humidity. The Arden-Buck equation provides the saturation pressure of water vapor [20], and is used to convert the 1000 mm pathlength in ambient air into its equivalent pathlength with respect to 37 °C and 100% relative humidity. The Arden-Buck equation is given in Eq. 10, where p is the pressure in atmospheres, and T the temperature in °C.

$$p = 6.032 \times 10^{-3} \exp\left(\frac{17.502\,T}{240.97 + T} \right) \tag{10}$$

#109769 - $15.00 USD Received 7 Apr 2009; revised 4 May 2009; accepted 5 May 2009; published 15 Jun 2009

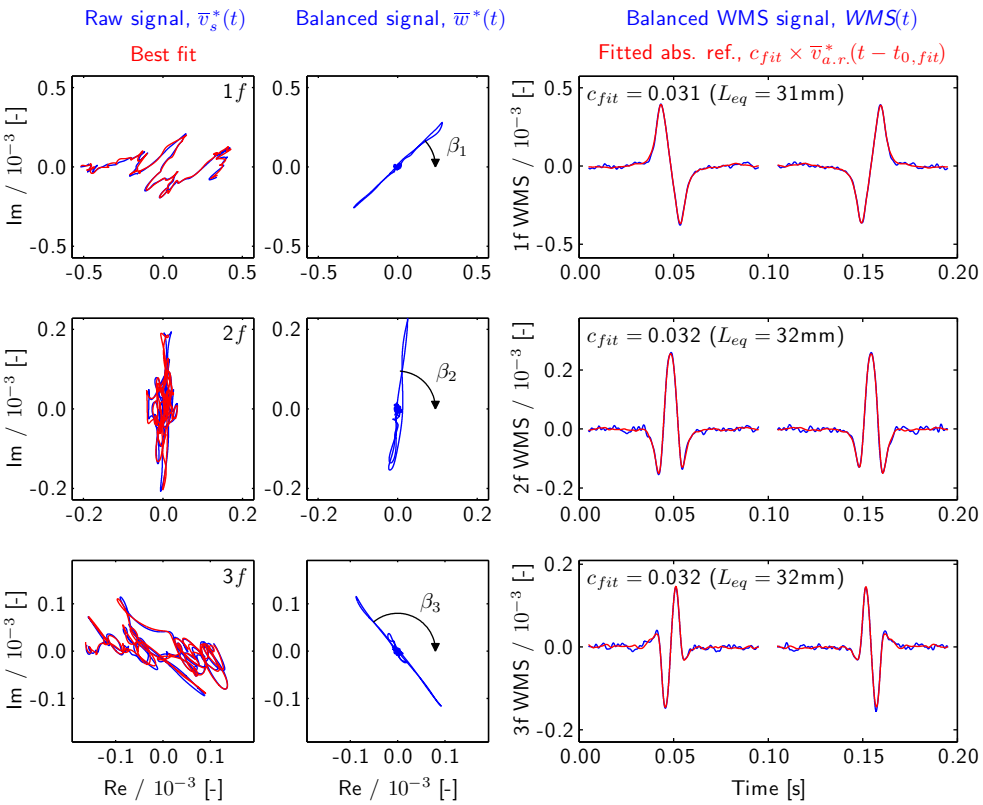

Fig. 4. Background subtraction exemplified using clinical data (molecular oxygen in the frontal sinus). Due to the triangular modulation used for laser modulation, each scan (dataset) include two interactions with the absorption feature. Differences in laser response in up- and downwards scanning requires that the imprints are evaluated separately. Despite fairly strong absorption, the absorption imprint is heavily distorted by background signals (left column). The observed structure can, however, be explained by the model in Eq. 6. Line-type phase-amplitude plot is obtained after background subtraction (middle column), and the resulting WMS signals (right column) exhibit good signal-to-noise ratio. The absolute reference was recorded on 1000 mm path of ambient air, and $c_{fit} = 0.032$ thus suggest an absorption that corresponds to 32 mm in air, *i.e.* 9×10^{-4} in absorption fraction ($L_{eq} = 32$ mm).

#109769 - $15.00 USD Received 7 Apr 2009; revised 4 May 2009; accepted 5 May 2009; published 15 Jun 2009

Note, for example, that a 150 mm pathlength at 37 °C and 100% relative humidity generates the same absorption of water vapor as a 1000 mm pathlength at 25 °C and 30% relative humidity (*i.e.* typical laboratory conditions).

2.3. Water vapor as a reference gas

The equivalent mean path length, L_{eq}, is of course dependent on both gas concentration and pathlength through gas. Since the pathlength is unknown in GASMAS, it is generally not possible to determine gas concentration. This complication may be circumvented if one performs simultaneous measurements on a gas with known concentration. For sinus diagnostics, water vapor has been used for this purpose [8]. If (i) the concentration of oxygen in the sinuses equals the atmospheric concentration, (ii) the optical properties (scattering and absorption) is the same at the two wavelengths used, and (iii) the gas in the sinus is at 37 °C and 100% relative humidity, $L_{eq}^{O_2}$ should equal $L_{eq}^{H_2O}$. Unfortunately, since water vapor is measured at 935 nm and oxygen at 760 nm, differences in equivalent pathlengths may be assigned to differences in optical properties rather than a change in oxygen concentration. Nonetheless, the ratio of the two has proven to be fairly stable [8]. In this work we employ photon time-of-flight spectroscopy (PTOFS) to investigate differences in optical properties (see below in Sect. 2.4 and Sect. 3.3).

2.4. Photon time-of-flight instrumentation

Differences in light propagation between 760 nm to 935 nm is studied by employing photon time-of-flight spectroscopy (PTOFS). The utilized system has been described in detail elsewhere, and has for example been used for *in vivo* spectroscopy of human prostate tissue [21, 22]. Briefly, the system is based on pulsed diode lasers and time-correlated single photon counting. Picosecond laser pulses are injected into the tissue, and transmitted diffuse light is collected and resolved in time. The obtained photon time-of-flight histograms can be used to determine optical pathlengths, average absorption and scattering coefficients. The two diode laser used operate at 786 nm and 916 nm, respectively, thus only slightly deviating from the two wavelengths used for the gas spectroscopy.

3. Results

3.1. System performance

The general system performance was analyzed by investigating how well the system can resolve differences in pathlength through ambient air. The results for the $2f$ harmonic are presented in Fig. 5, and show that the precision is on the order of 1 mm. The performance varies slightly between the different harmonics, as reported also in Ref. [7]. Such effects may be assigned to problems of interference fringes occurring in experiments involving source-detector separations in the mm range. For example, the free spectral range of a 50 mm air etalon matches the width of the absorption linewidth (at atmospheric conditions), and may therefore be detrimental to the measurement.

3.2. Clinical data

Clinical data are acquired at the Radiology Clinic of the Lund University Hospital, within the framework of a clinical study aimed at comparing laser-based gas sensing with conventional CT diagnostics. The study is approved by the local committee of ethics, and patients are enrolled after informed consent. The maxillary sinuses, behind the cheekbone, are studied by placing the fiber probe in contact with one side of the mouth cavity roof, close to the sinus under study. The diffuse light is detected on the cheekbone. To monitor the frontal sinuses, behind the frontal bone, the fiber probe is placed under one side of the eyebrow, close to the nasal bone, injecting

#109769 - $15.00 USD Received 7 Apr 2009; revised 4 May 2009; accepted 5 May 2009; published 15 Jun 2009

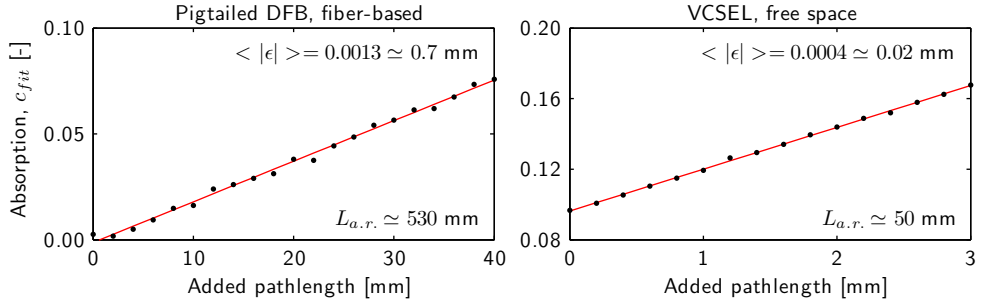

Fig. 5. Investigation of system performance by measurements on series of distances of ambient air ($2f$ signals, molecular oxygen). When using the fiber-based clinical system, the resolution is about 1 mm L_{eq}, *i.e.* about 3×10^{-5} (average absolute deviations from the fitted line, $< |\varepsilon| >$). The resolution is significantly better, about 0.02 mm L_{eq}, when the optical system is replaced with a non-collimated VCSEL and a single large-area photodiode (this system is described and used in Refs. [5, 7]). For this series, note the initial pathlength offset of about 5 mm.

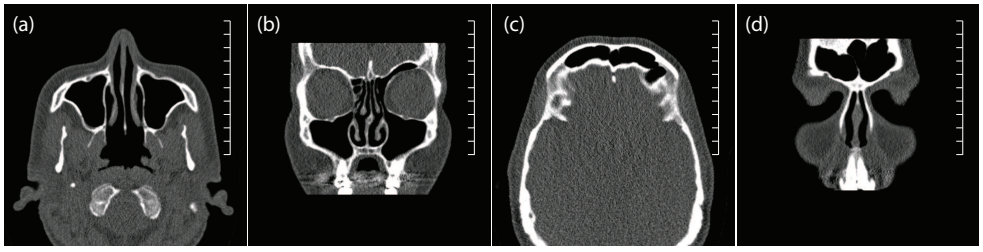

Fig. 6. CT images of the maxillary (a-b) and frontal sinuses (c-d). Black areas surrounded by white borders (bone) correspond to air filled cavities. Each division on the scale corresponds to 1 cm.

the light up in the frontal bone. The scattered light is detected on the forehead, with the bottom part of the detector located about 1 cm above the eyebrow. Light is acquired during 20 s (100 scan averages). Ambient light sources are turned off or blocked during the measurement.

Figure 6 shows CT images of the frontal and maxillary sinuses of one of the patients enrolled in the clinical study. The results of gas measurements on this particular patient is given in Fig. 7 (frontal sinuses) and Fig. 8 (maxillary sinuses). The signal-to-noise ratio, *SNR*, is calculated by taking the ratio of the WMS peak and the maximum absolute value of fit residuals. The SNR obtained suggest a detection limit of about 2 mm for both oxygen and water vapour (when using the $1f$ or $2f$ harmonics). This corresponds to absorption fractions of about 5×10^{-5} for oxygen and 5×10^{-4} for water vapour. The measurement resolution is better than the maximum residual value, and is thus expected to be significantly better than 2 mm. It should, however, be noted that the performance varies between patients due to large variations in light attenuation. The improvement in signal quality, with respect to earlier clinical data, is significant [18].

3.3. Photon time-of-flight data

The results of photon time-of-flight (TOF) experiments are reported in Fig. 9 and Tab. 1. The total optical pathlength is on the order of 100 mm, but varies strongly. Clearly, there are significant differences with respect to light propagation between the two wavelengths used for gas

#109769 - $15.00 USD Received 7 Apr 2009; revised 4 May 2009; accepted 5 May 2009; published 15 Jun 2009

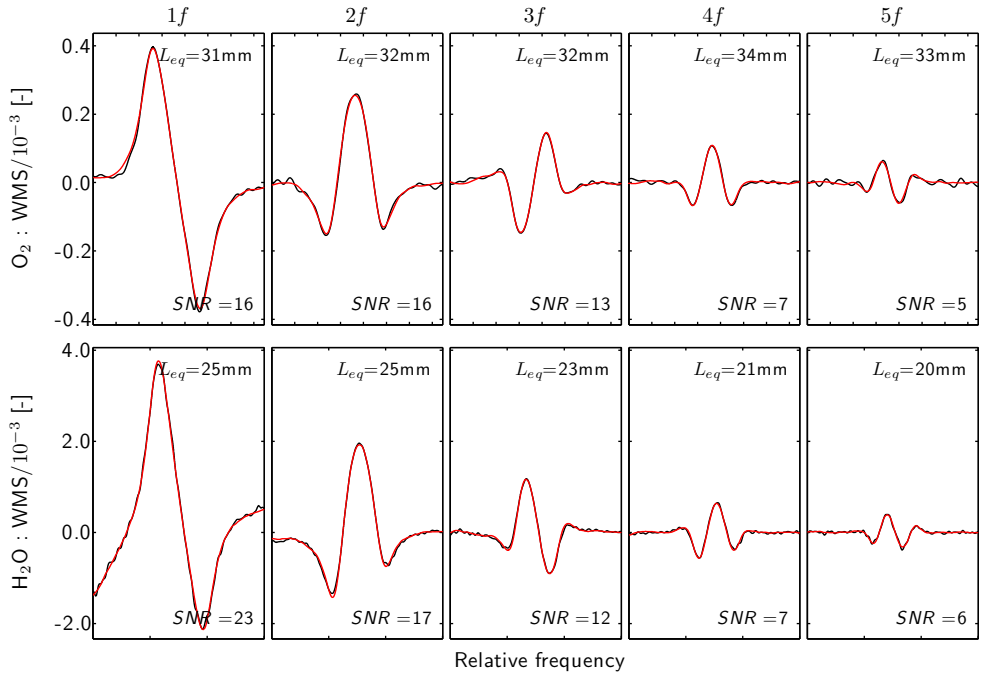

Fig. 7. 1-5f WMS signals from measurements on the left frontal sinus of a patient (black) together with fitted absolute reference data (red). CT images of this frontal sinus is found in Fig. 6. The detected power was 9 μW for 760 nm and 1 μW for 935 nm (transimpedance amplification was set to 10^6). The slightly lower L_{eq} for water vapor is typical, and is investigated in Sect. 3.3. Note the weak signal strength at higher harmonics, reducing the signal-to-noise ratio and causing increased uncertainty in L_{eq} estimation. Note also that the water absorption is about ten times stronger than the oxygen absorption.

spectroscopy. The data suggests that light used for oxygen sensing (760 nm) travels between 30 and 50% longer than light used for sensing of water vapour (935 nm). This fact explains why $L_{eq}^{H_2O}$ typically is systematically lower than the $L_{eq}^{O_2}$ (see *e.g.* Fig. 7). The differences between the two L_{eq}-values are, however, typically lower than the 30-50% implied by PTOFS. This discrepancy can be assigned to the non-trivial division of the total pathlength between tissue and sinus cavity. Considering the complexity of light propagation in strongly heterogenous materials such a discrepancy is not unexpected. The issue may deserve further attention, and could be studied by Monte Carlo simulation.

Since the geometry of sinus measurements is complex and unknown, no appropriate model for light propagation is available. However, at late photon time-of-flights, the shape of the TOF distribution is mainly governed by the Beer-Lambert-Bouguer exponential decay $\exp(-\mu_a ct)$, where μ_a is the absorption coefficient, and c the speed of light in the medium. Absorption coefficients can thus be estimated from the decay of the TOF distribution (the final slope of the intensity plotted in log-scale) [23]. This estimation should, however, be considered rough, since geometry and scattering properties greatly influence its accuracy [9].

#109769 - $15.00 USD Received 7 Apr 2009; revised 4 May 2009; accepted 5 May 2009; published 15 Jun 2009

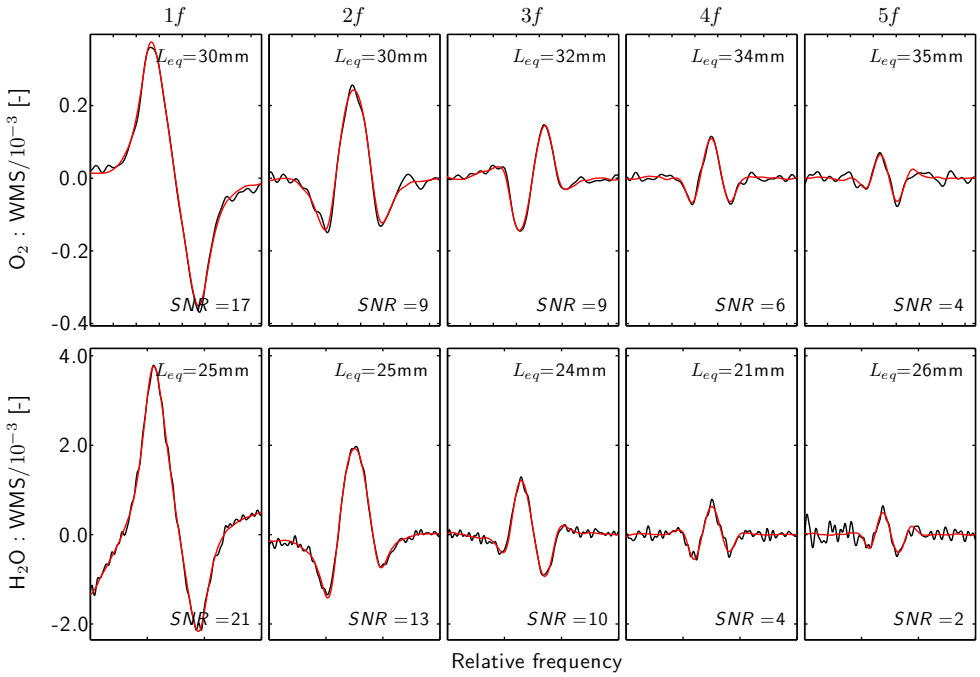

Fig. 8. 1-5f WMS signals from measurements on the left maxillary sinus of a patient (black) together with fitted absolute reference data (red). CT images of this maxillary sinus is found in Fig. 6. The detected power was 2.7 μW for 760 nm and 0.15 μW for 935 nm (transimpedance amplification was set to 10^6).

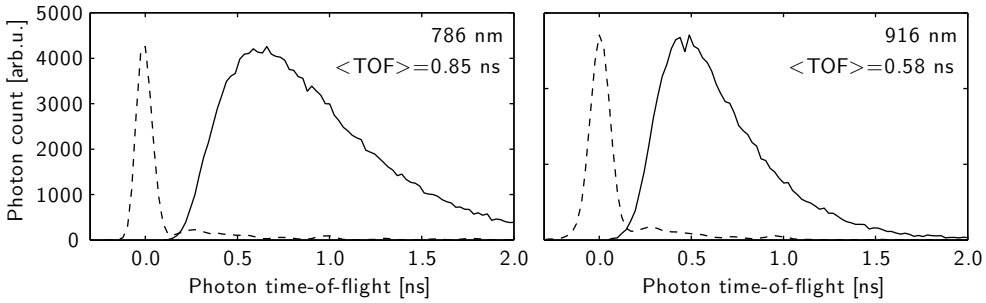

Fig. 9. Photon time-of-flight distributions obtained from measurements on the maxillary sinuses. A measurement of the instrumental response function (dashed) provides the origin for the absolute time scale.

#109769 - $15.00 USD Received 7 Apr 2009; revised 4 May 2009; accepted 5 May 2009; published 15 Jun 2009

	Mean TOF [ns]		Mean path [mm]		Abs. coeff. [cm^{-1}]	
	786 nm	916 nm	786 nm	916 nm	786 nm	916 nm
Volunteer 1, Frontalis	0.54	0.40	116	86	0.13	0.16
Volunteer 1, Maxillaris	1.38	0.90	296	193	0.10	-
Volunteer 2, Frontalis	0.61	0.45	131	97	0.11	0.14
Volunteer 2, Maxillaris	0.85	0.58	182	125	0.10	0.16

Table 1. Photon pathlengths and estimations of average absorption coefficients, as obtained from PTOFS. Mean pathlengths are calculated from mean TOF, assuming a refractive index of 1.4. For the measurements on the maxillary sinuses of volunteer 2, low light transmission prevented proper analysis of absorption coefficient.

4. Discussion

The system described in this work is clearly capable of providing useful clinical data on the gas contents of human paranasal sinuses. There are, however, alternative system designs that could achieve similar or even better performance. The advantages of using optical fibers to deliver light is the straight forward construction of an appropriate medical probe. In addition, fibers allow convenient coupling of different light sources, rendering the use of multiple light sources fairly simple. The major drawback, however, is that the use of pigtailed diode lasers and optical fibers appears to degrade the system performance. Despite the elaborate schemes for background suppression described in this paper, the performance is still significantly poorer than comparable single-beam systems that avoid optical fibers [5, 9]. However, considering for example the high sensitivity fiber-based gas sensor developed by Engelbrecht [24], we expect that we can improve our current fiber-based system. Nonetheless, the possibilities of constructing a single-beam system, avoiding pigtailing and optical fibers, should be investigated. Potential advantages include reduced system complexity, significant cost reduction, as well as simpler and more robust data evaluation. The small size of diode lasers renders it possible to construct a medical probe that injects light directly from the output of the diode lasers. The ideal solution would be a single diode laser capsule that contains different diode lasers, operating at different wavelengths. Furthermore, replacing pigtailed DFB-lasers with *e.g.* VCSEL lasers (shown feasible in Ref. [14]) would make the system much more cost-efficient.

Another issue that deserves some attention is that the access to multiple WMS harmonics reveals some technical imperfections. We have observed discrepancies between the L_{eq}-values obtained from the different harmonics. Water vapor appears to be particularly affected. Possible technical explanations include differences in detector response with harmonic frequency and light distribution over the large-area photodiode. We are also investigating whether differences in conditions between the measurements of absolute references and the actual clinical measurements can effect system behavior. In order to determine and improve measurement accuracy, these effects require further attention.

Finally, since high light attenuation may degrade the sensitivity, the values given for detection limit show be considered as guidelines. Nonetheless, a look through the full clinical dataset shows that 2 mm L_{eq} most often is a fair indication of the limit of detection. We will discuss this important aspect in detail in a forthcoming article that will focus on the clinical data.

Acknowledgment

This work was supported by The Swedish Research Council through a project grant and a Linnaeus Grant for the Lund Laser Centre. the Knut and Alice Wallenberg Foundation, as well as by the Medical Faculty, Lund University. The authors also gratefully acknowledge Prof.

Stefan Andersson-Engels for the collaboration on time-of-flight spectroscopy, as well as Prof. Sven Lindberg, Prof. Kjell Jonson and Dr. Roger Siemund at the Lund University Hospital for supporting and assisting in the clinical work.

#109769 - $15.00 USD Received 7 Apr 2009; revised 4 May 2009; accepted 5 May 2009; published 15 Jun 2009